OPTICAL CONSTANTS AND BAND STRENGTHS OF CH$_4$:C$_2$H$_6$ ICES IN THE NEAR- AND MID-INFRARED

GERMÁN MOLPECERES[1], MIGUEL ANGEL SATORRE[2], JUAN ORTIGOSO[1], CARLOS MILLÁN[2], RAFAEL ESCRIBANO[1], AND BELÉN MATÉ[1]

[1] Instituto de Estructura de la Materia, IEM-CSIC, Serrano 123, E-28006 Madrid, Spain; belen.mate@csic.es
[2] Escuela Politécnica Superior de Alcoy, UPV, E-03801 Alicante, Spain

ABSTRACT

We present a spectroscopic study of methane–ethane ice mixtures. We have grown CH$_4$:C$_2$H$_6$ mixtures with ratios 3:1, 1:1, and 1:3 at 18 and 30 K, plus pure methane and ethane ices, and have studied them in the near-infrared (NIR) and mid-infrared (MIR) ranges. We have determined densities of all species mentioned above. For amorphous ethane grown at 18 and 30 K we have obtained a density of 0.41 and 0.54 g cm^{-3}, respectively, lower than a previous measurement of the density of the crystalline species, 0.719 g cm^{-3}. As far as we know this is the first determination of the density of amorphous ethane ice. We have measured band shifts of the main NIR methane and ethane features in the mixtures with respect to the corresponding values in the pure ices. We have estimated band strengths of these bands in the NIR and MIR ranges. In general, intensity decay in methane modes was detected in the mixtures, whereas for ethane no clear tendency was observed. Optical constants of the mixtures at 30 and 18 K have also been evaluated. These values can be used to trace the presence of these species in the surface of trans-Neptunian objects. Furthermore, we have carried out a theoretical calculation of these ice mixtures. Simulation cells for the amorphous solids have been constructed using a Metropolis Monte Carlo procedure. Relaxation of the cells and prediction of infrared spectra have been carried out at density functional theory level.

Key words: methods: laboratory: molecular – planets and satellites: composition – techniques: spectroscopic

Supporting material: data behind figures

1. INTRODUCTION

Methane and ethane are constituents of planetary ices in our solar system. Methane has been detected in outer solar system bodies like Titan, Pluto, Charon, Triton, or other trans-Neptunian objects (TNOs; Cruikshank et al. 1976; Barucci et al. 2005; Brown et al. 2006; Licandro et al. 2006; Dalton et al. 2010a; Cruikshank et al. 2015). Ethane, a product of energetic processing of methane (de Vries et al. 1984; Kaiser & Roessler 1992; Strazzulla et al. 2002), has also been identified in some of those objects (Schaller & Brown 2007; Dalle Ore et al. 2009; DeMeo et al. 2010; Merlin et al. 2010; Cruikshank et al. 2015).

The NASA *New Horizons* spacecraft did its close-up flyby of Pluto on 2015 July 14. Since then, its Ralph instrument is providing very high quality near-infrared (NIR) spectra of the surface of the planet (1.25–2.5 μm with 240 resolution and 2.1–2.25 μm with 560 resolution). The NIR spectra will inform about the molecular ices present on Pluto's surface. Detailed laboratory spectroscopic data of the possible chemical species present in those systems are needed for the interpretation of the observed spectra. Necessary information includes band positions and band strengths, and also complex refractive indices for the evaluation of scattering, reflection, and absorption spectra of condensed species. The motivation of our work was to provide new laboratory data that may contribute to the understanding of those systems, in the new era of knowledge of TNOs opened up by the *New Horizons* mission.

There are many laboratory measurements on the infrared spectra of pure CH$_4$ and C$_2$H$_6$ ices (Pearl et al. 1991; Hudgins et al. 1993; Hudson et al. 2014; Gerakines & Hudson 2015). Under vacuum conditions methane ice presents three phases. The high-temperature phase (phase I) is a crystalline solid with a high degree of rotational disorder, while the low-temperature crystalline phase (phase II) has a more ordered structure. A

reversible transition between both phases takes place around 20 K (Clusius 1929). The amorphous phase is formed in the laboratory by vapor deposition at low temperature (below 15 K) and at very low deposition rates (Gerakines & Hudson 2015). However, it has been observed that the low-temperature crystalline phase can be obtained by deposition at temperatures as low as 10 K, depending on the growing conditions. The infrared spectra of ethane ice have also been studied (Pearl et al. 1991; Quirico & Schmitt 1997). Below 90 K ethane presents three phases: amorphous, crystalline, and metastable (Hudson et al. 2014). The amorphous phase is formed by slow deposition below 20 K. Condensation at higher temperatures gives the metastable form (between 30 and 50 K) and the crystalline form (60–70 K) (Wisnosky et al. 1983).

We have focused the present investigation on the spectroscopic study of methane–ethane ice mixtures. We have grown CH$_4$:C$_2$H$_6$ mixtures with ratios 3:1, 1:1, and 1:3 at 18 and 30 K, plus pure methane and ethane ices. Although the temperature of Pluto's surface lies between 40 and 50 K, and that of Charon is around 53 K, methane sublimates at 40 K under our experimental conditions. We therefore decided to work at 30 K, a temperature low enough to guarantee no sublimation of methane but close to the higher temperatures in the outer solar system bodies. Experiments at lower temperature, 18 K, have also been conducted to check how temperature affects the results. We have covered the NIR and mid-infrared (MIR) ranges searching for possible modifications of the spectra of the pure species in the mixtures. Our results include band positions, optical constants, and band strengths, based on new measurements of ice densities and optical refractive indices, for the pure species and the mixtures investigated. Comparison with earlier works on the pure species is also provided. As far as we know, there is no previous literature information on the mixtures investigated

here, but comparisons with results on mixtures of CH_4 or C_2H_6 with other species are discussed when available. Furthermore, we present in this work a theoretical calculation of these ice mixtures, which includes a prediction of their MIR spectra. Finally, the astrophysical implications of our work are discussed.

2. METHODOLOGY

2.1. Experimental Setup

The experimental setup has been described in detail in previous works (Satorre et al. 2013; Zanchet et al. 2013), although some improvements have been introduced for this study. Basically, the setup at IEM in Madrid consists of a high vacuum chamber that works in the 10^{-8} mbar range, provided with a closed helium cycle cryostat and coupled to a Bruker Vertex 70 FTIR spectrometer. An IR transparent silicon substrate suited to work in transmission configuration was placed in a copper holder in close contact with the cold head of the cryostat. The holder leaves a front and a back surface of 1 cm diameter of the Si buffer uncovered. The substrate temperature can be controlled between 18 and 300 K with 0.5 K accuracy by means of a Lakeshore temperature controller linked to two calibrated silicon diodes. A silicon diode is placed at the bottom part of the holder, and the other at the end of the cold cryostat head, both measuring the same temperature within 0.5 K. For this investigation the substrate was kept at 18 K or 30 K and the gases, CH_4 (99.95% Air Liquide) or C_2H_6 (99.5% Air Liquide), were introduced into the chamber through independent lines. The gas inlet lines, 6 mm in diameter, are placed in the same DN40CF flange in a chamber port situated 10 cm below the optical path plane, ensuring backfilling the chamber with homogeneous pressure. Mass flow controllers (Alicat) were mounted in each gas line to ensure a high stability and reproducibility in the growing conditions of the pure ice species and mixtures. The samples were condensed at deposition rates between 3.6 and 7.2 μm hr^{-1} and allowed to grow to thicknesses between 0.5 and 6.0 μm. These values include the two layers that grow one at each side of the substrate. Ice thickness was measured following the interference pattern of an He–Ne laser (628 nm) in quasi-normal (4° angle) reflection configuration. The geometry of both the chamber and the Si holder was especially designed to obtain a symmetric deposition on both sides of the substrate. This was confirmed by monitoring with the He–Ne laser the desorption of the back-side deposit. Transmission spectra in the MIR (4000–500 cm^{-1}) and NIR (8000–3000 cm^{-1}) regions were recorded with 2 and 1 cm^{-1} resolution, respectively, in normal incidence, with 200 co-added scans. Spectra of pure CH_4 were recorded at 0.5 cm^{-1} in order to identify properly the crystalline phase II. The lamp and beamsplitter were changed to record the spectra in each spectral range, keeping the same MCT detector.

To measure refractive index and density, experiments were carried out in the Laboratory of Characterizations of Astrophysical Ices at Alcoy. The experimental procedure and setup are the ones described in Satorre et al. (2013). Ices were grown in a high vacuum chamber with the same characteristics as used for the IR spectra. For these experiments, a quartz crystal microbalance (hereafter QCMB) was used as a sample holder to measure the mass deposited per square centimeter, and two

interferometric He–Ne signals impinging on the flat QCMB surface allow us to obtain the refractive index (and then the thickness) of the deposited ice. The estimated accuracy for the QCMB temperature is below 1 K at 18 K and below 0.5 K at 30 K. Differences in ice growing temperatures between the two laboratories should be below 1 K, and these variations affect the results well below the experimental errors considered. Pure compounds and mixtures of methane (Praxair 99.9995%) and ethane (Praxair 99.95%) were prepared in a prechamber and introduced into the vacuum chamber through a needle valve. Gases filling the chamber were not directed to the QCMB surface, in a background deposition setup. A constant pressure in the vacuum chamber ensures a uniform deposition rate yielding a constant slope on the QCMB and in a quadrupole mass spectrometer, also used to control contaminant levels during deposition. For most of the experiments the deposition rate at 18 and 30 K was 3 nm s^{-1}. Sample thickness for these experiments varied between 2 and 3 μm.

Concerning the effect of the growth rate on the phase of the pure ices, we found that for samples deposited at 18 and 30 K deposition rates between 0.1 and 3 nm s^{-1} do not affect significantly the IR spectra, in terms of intensities or band profiles. Rates between 1 and 13 nm s^{-1} do not induce variations on density or refractive index either.

To determine the optical constants and band strengths in the MIR, we have used spectra of ices below 1.4 μm in thickness only, in order to avoid saturation of the strongest features. In the NIR region spectra of films between 2 and 6 μm thick were employed.

2.2. Theoretical Method

We have carried out quantum chemical calculations of models of the aforementioned mixtures in order to support the validity of our results.

Several simulation cells have been constructed using a Metropolis Monte Carlo procedure, as implemented in the Amorphous Cell module of the Materials Studio suite of programs (http://accelrys.com/products/materials-studio/, 2014). These simulation cells have been built packing four molecules (3+1, 2+2, and 1+3 of CH_4 and C_2H_6) inside them and setting the density of the system to match the measured densities of each mixture. Once the cell was ready, a density functional theory (DFT) relaxation of the structures using sequentially tighter convergence criteria was performed. The final convergence parameters were set to 5×10^{-6} eV atom^{-1} for the energy, 0.01 eV Å^{-1} for the gradient of the energy, and 5×10^{-4} Å for the maximum displacement in the atomic positions. The DFT relaxation was done in the GGA (Generalized Gradient Approximation) context using the Perdew–Burke–Ernzerhof functional (Perdew et al. 1996). All the calculations have been performed using a plane-wave, pseudopotential method. Cutoff energy for the plane-wave expansion was 900 eV, and norm-conserving pseudo-potentials were chosen. A Grimme dispersion correction was also applied (Grimme 2006). Once the structures were relaxed, infrared spectra were computed within the harmonic approximation limit. All the DFT calculations were carried out using the CASTEP (Clark et al. 2005; Refson et al. 2006) code.
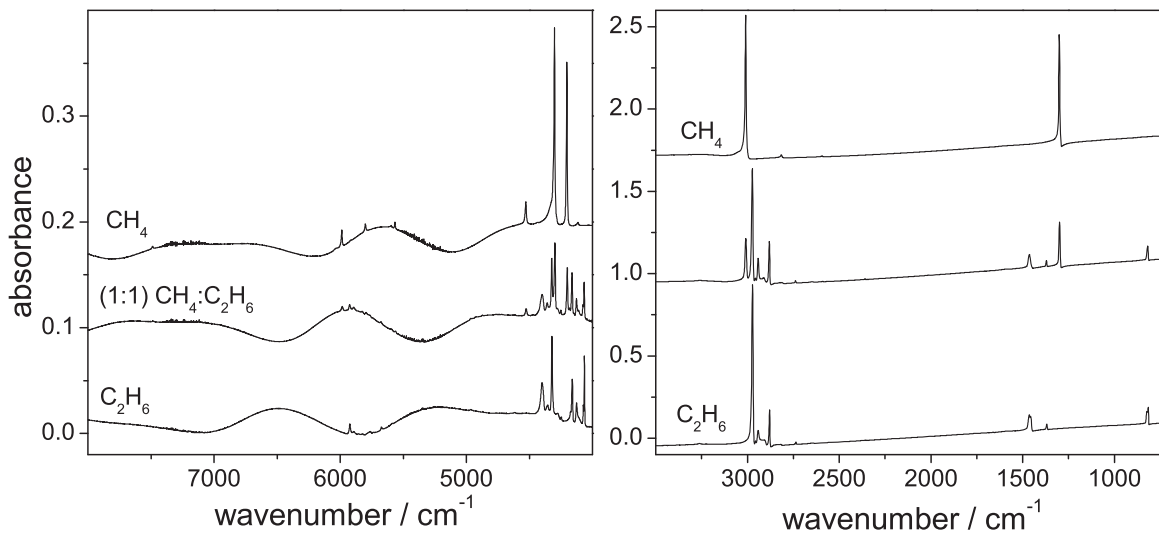
Figure 1. IR spectra of a (1:1) CH_4:C_2H_6 mixture, pure CH_4, and pure C_2H_6 at 18 K. Left: NIR, ice thickness $\sim$6.5 μm; right: MIR, ice thickness $\sim$1.4 μm. The spectra have been offset for clarity. Data used to create this figure are available.
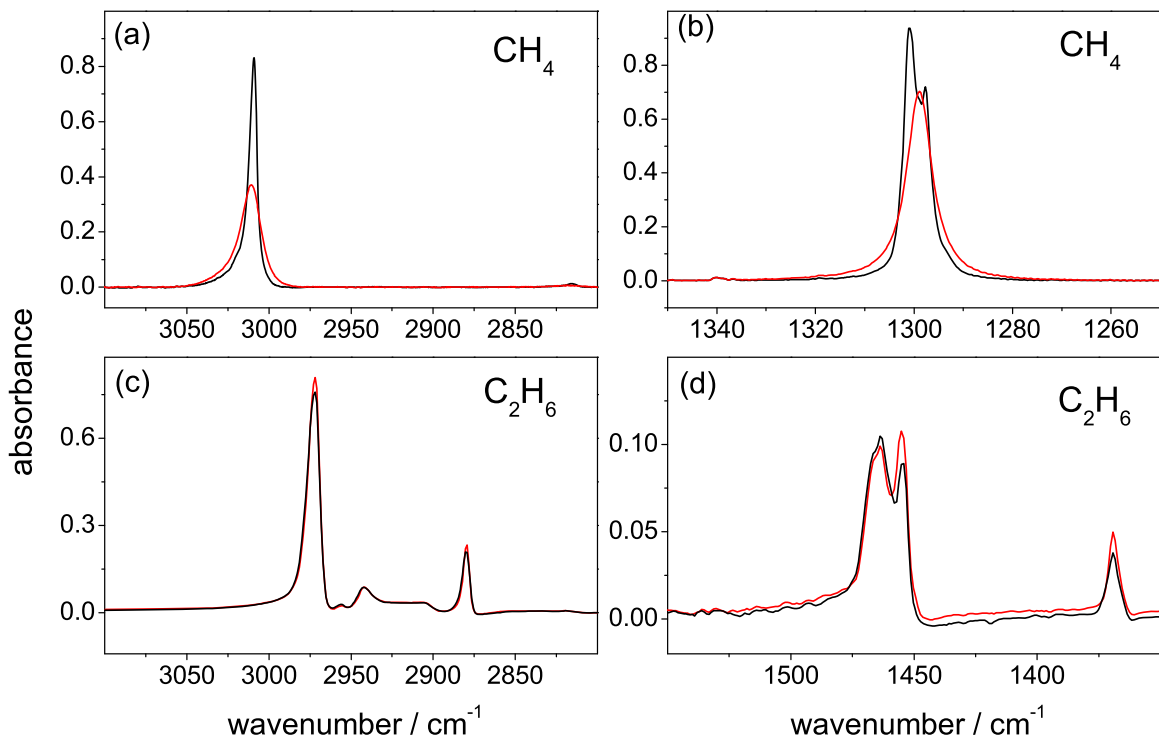

Figure 2. MIR spectra of 1.4 μm ice layers of CH_4 (top panels) and C_2H_6 (bottom panels) grown at 18 K (black) and 30 K (red). Methane spectra have 0.5 cm^{-1} resolution.

3. RESULTS

3.1. NIR and MIR Spectra of Pure Species and CH4:C2H6 Mixtures

Spectra of a (1:1) CH_4:C_2H_6 mixture, pure CH_4, and pure C_2H_6 are represented in Figure 1, for the NIR and MIR regions (left and right panels, respectively). NIR spectra correspond to ice thicknesses of about 6.5 μm and MIR spectra to ice layers of about 1.4 μm. These thicknesses refer to the sum of two layers, one at each side of the IR transparent substrate. The undulations in the baseline, clearly evidenced in the NIR spectra, are due to IR interferences.

Selected MIR spectral regions of pure methane and ethane are shown in Figure 2 to illustrate the ice phases of the pure samples obtained at the experimental conditions of the present work. As expected, for methane ice grown at 30 K we have rotationally disordered crystalline phase I, which presents a symmetric band profile for both the ν_3 and ν_4 modes, at 3010 and 1300 cm^{-1}, respectively (red trace, panels (a) and (b)). When methane ice is grown at 18 K (black trace), the profiles of these modes becomes narrower and, at 0.5 cm^{-1} resolution, a splitting of the ν_4 mode is appreciated, which is characteristic of the low-temperature phase II (Gerakines & Hudson 2015).
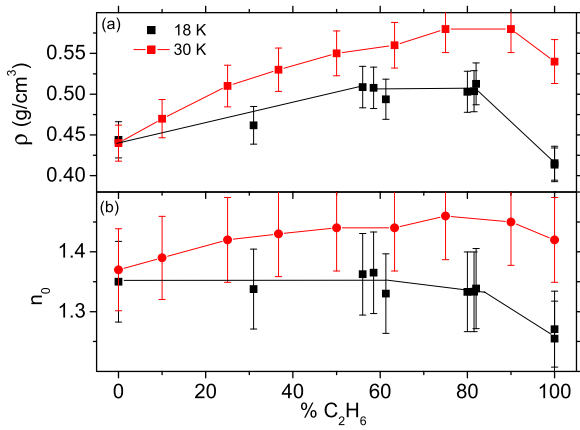
Figure 3. Density and visible refractive index of CH_4:C_2H_6 mixtures at 18 and 30 K.

Ethane ice grown at 18 and 30 K is amorphous, perhaps with some contamination of the metastable phase as evidenced by the unresolved double peak in the ν_3 mode at $1464\,cm^{-1}$ (panel (d)). This double peak was not observed in the spectrum of amorphous ethane grown at 12 K and then warmed to 20 K reported by Hudson et al. (2014). Wisnosky et al. (1983) suggested that the metastable phase of ethane is formed when the ice is grown between 30 and 55 K. In our experiments we found that some metastable phase starts to be formed at lower temperatures.

3.2. Density and n_0

Figure 3 displays the density and visible refractive indices of pure CH_4, C_2H_6, and CH_4:C_2H_6 mixtures at 18 K. Density is a very interesting property of ices since it is related to the possible porosity in amorphous samples, and it can also be used to trace phase changes. Moreover, it is needed to estimate correct IR band strength coefficients for each individual sample, since the amount of detected absorbed radiation depends directly on the density of the sample. As for the refractive index, the measured values are required as input parameters for optical constant determinations and interferometric He–Ne laser film thickness determinations. Starting from pure crystalline methane, with density $0.45\,g\,cm^{-3}$, a slight compaction of the samples is observed with increasing ethane concentration. However, at the other end of the graph, pure amorphous ethane has lower density than the mixtures. At 18 K it is even lower than that of pure methane. As far as we know, the only available literature value for ethane ice density is much larger, $0.719\,g\,cm^{-3}$, and corresponds to its crystalline phase (Van Nes & Vos 1979) at 85 K. For pure methane, the present value coincides within experimental error with the one published by Satorre et al. (2008).

We can put forward a possible explanation for these effects. As we have mentioned above, methane is crystalline at 18 and 30 K, while ethane ice is amorphous at these temperatures. On one hand, in order for methane to accommodate the larger ethane molecules, its crystalline structure must be shattered, allowing the two kinds of molecules to get closer and form a compact solid, thus making the ice mixture denser. On the other hand, pure amorphous ethane seems to have holes in its structure that are easily filled with methane in diluted methane mixtures, increasing the density of the solid mixture. The behavior is similar at 18 and 30 K.

3.3. Comparison of Spectra

Infrared spectra in the $6100–700\,cm^{-1}$ spectral range of the ice samples investigated in this work are presented in Figure 4. An adequate baseline has been subtracted to improve the representation and help in comparing them. Figure 4(a) displays the spectra of the pure species and of a (1:1) CH_4:C_2H_6 mixture, while Figure 4(b) collects the spectra of the mixtures. Although the spectra of pure samples are well known, it is illustrative to compare them to identify the features that correspond to each species and to illustrate the spectral changes that take place upon mixing. For instance, the strong band at $3008\,cm^{-1}$ corresponds to the CH_4 asymmetric C–H stretch (ν_3), being shifted to $2970\,cm^{-1}$ for C_2H_6, and the strong methane bending at $1300\,cm^{-1}$ can be ascribed to the weak ethane peak at $1380\,cm^{-1}$. In general, the ethane bands in the (1:1) mixture are closer in intensity to those of pure ethane, while those of pure methane look stronger, although the ices have the same thickness. The interpretation of this behavior is difficult since intensities are affected by the combination of two effects: different sample densities and modification of intrinsic band strengths in the mixture, as will be discussed below. Wavenumber shifts and band shape modifications are easily observed in the spectra of both Figures 4(a) and (b). In particular, we can mention that the pure ethane doublets at $823–815\,cm^{-1}$ and $1460–1450\,cm^{-1}$ become single bands in the mixtures. Perhaps more relevant for astronomical observations is the C_2H_6 band at $4400\,cm^{-1}$ that modifies appreciably its profile in the mixtures. The single peak is transformed to a double peak in the most diluted C_2H_6 sample (see Figure 4(b)).

Figure 5 represents the displacement of the main NIR bands of either species as a function of dilution into each other. It is interesting to notice that methane bands shift to lower wavenumbers relative to the pure species, while ethane bands have in general the opposite behavior. The larger CH_4 shifts are measured at the 30 K experiment.

Hudgins et al. (1993) found large wavenumber displacements for the MIR bands of CH_4 in 20:1 (X:CH_4) mixtures with several volatiles, like X = CO, CO_2, H_2O, N_2, and O_2. In all cases the bands showed a shift to shorter wavelengths in the mixtures as compared with the pure species. Also Quirico & Schmitt (1997) and Gálvez et al. (2009) found that CH_4 peaks shift to higher frequencies when highly diluted in N_2 or in H_2O, respectively. On the other hand, for CH_4:H_2O ratios with large methane amount, the opposite behavior was reported, leading to a shift to longer wavelengths (see Figure 3 in Gálvez et al. 2009). In the CH_4:C_2H_6 mixtures investigated in this work, CH_4 peak positions move to lower frequencies for all dilutions.

As for C_2H_6, Quirico & Schmitt (1997) measured shifts to higher wavenumbers for a (1:100) (C_2H_6:N_2) mixture, and Boudin et al. (1998) observed the same tendency in (1:20) (C_2H_6:H_2O) and (C_2H_6:CO) mixtures, in agreement with the observations of this work.

3.4. Optical Constants n and k

The optical constants in the NIR and MIR regions were determined from normal incidence transmission spectra of ice layers of known thickness, making use of the visible refractive index, n_0, obtained from double interference measurements (see Section 2).

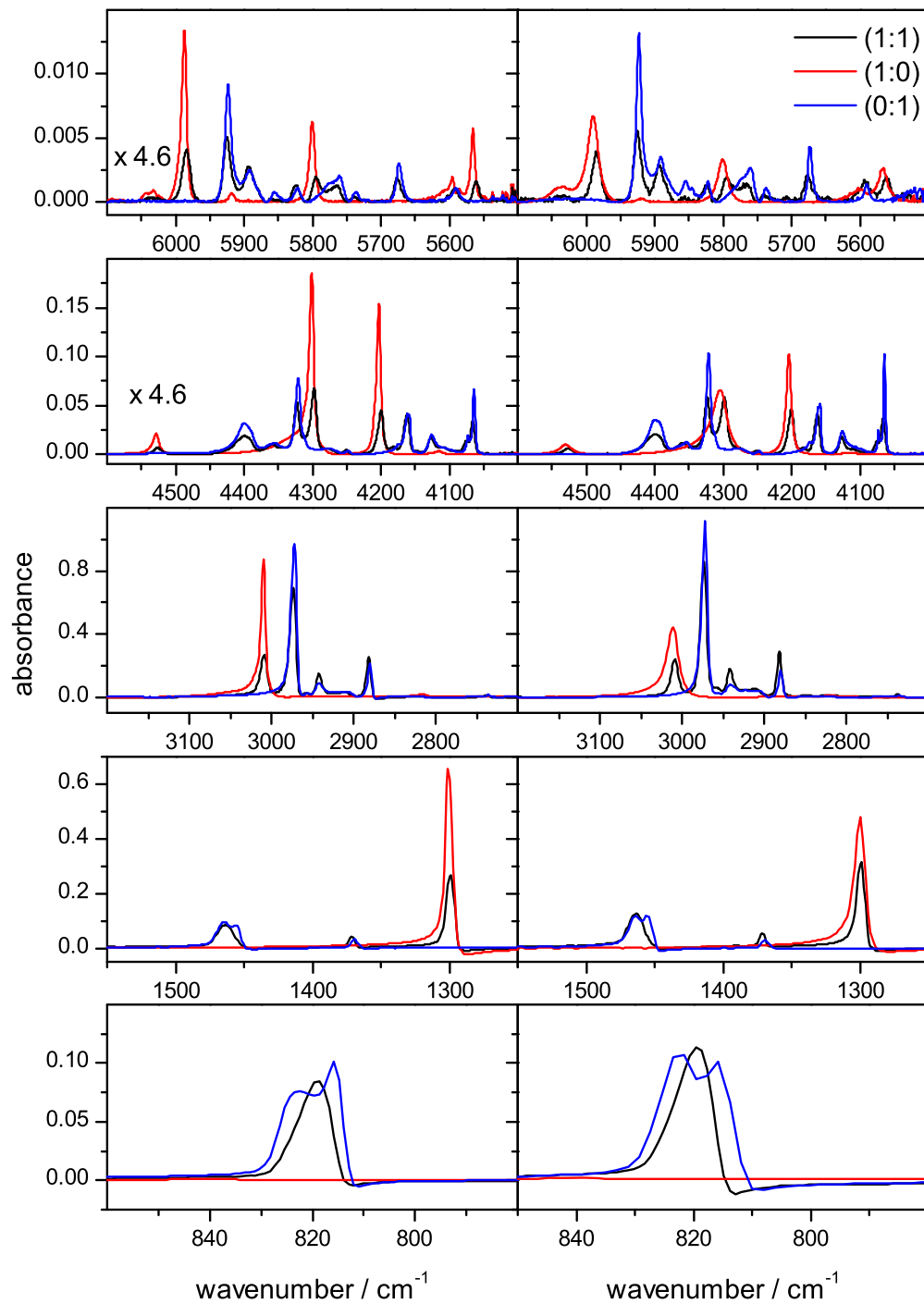The iterative fitting procedure described in Zanchet et al. (2013) was applied for MIR spectra. The method fits the

Figure 4. (a) IR spectra of pure CH_4 (1:0, red), pure C_2H_6 (0:1, blue), and a (1:1) mixture (black) grown at 18 K (left) and 30 K (right). Ice thickness is 1.4 μm in all cases. Baselines have been subtracted. (b) IR spectra of CH_4:C_2H_6 mixtures grown at 18 and 30 K. Ice thickness is 1.4 μm in all cases. Traces correspond to (3:1, red), (1:1, black), and (1:3, blue) CH_4:C_2H_6 mixtures. Baselines have been subtracted. Data used to create this figure are available.

thickness, coherence, n_0, n, and k to minimize a merit function that depends on the difference between experimental and calculated spectra. Only layers with thickness below 1.5 μm were used in order to avoid saturation of the strongest methane and ethane MIR absorption bands. The fitted thickness and n_0 are reproduced within less than 5% from their experimental values.

In the NIR a different methodology that does not involve any iterative fitting (Mastrapa et al. 2008; Zanchet et al. 2013) was employed. In this case, after subtracting an adequate baseline to

the absorbance spectra to remove IR interferences, k values are extracted via the Lambert–Beer law. Then, the real part of the refractive index is calculated from the Kramers–Kroning relation between n and k. Figure 6 shows the results for the tree mixtures investigated (at 18 K).

4. BAND STRENGTHS

The integrated band strengths have been calculated in two ways. On one hand, they were obtained by direct integration of
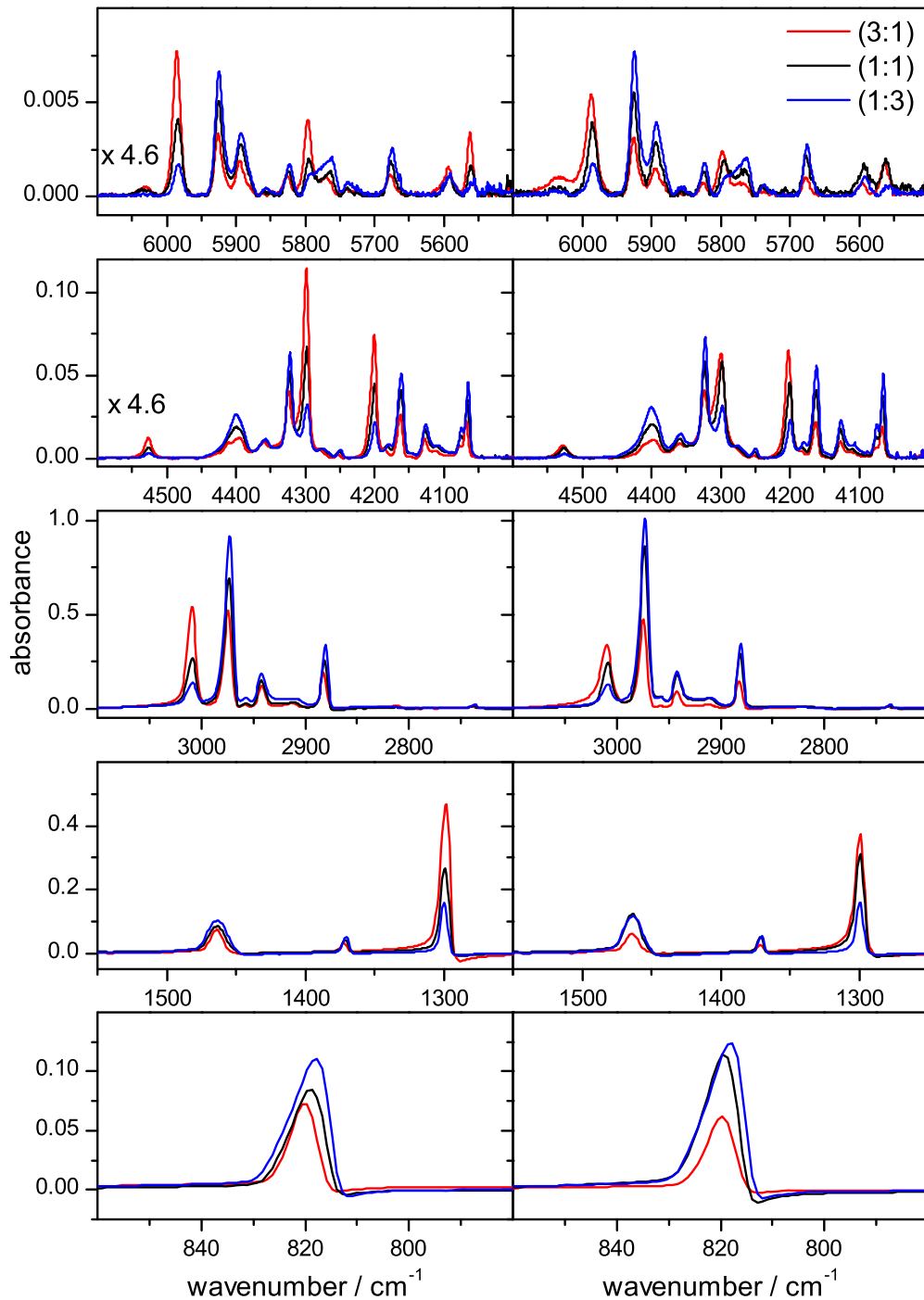
Figure 4. (Continued.)

the infrared absorption in the absorbance spectrum. The band strength is related to the integral through the expression

$$A' = 2.303 \frac{\int_{band} \alpha(v)\, dv}{\rho_X\, L}, \qquad (1)$$

where the numerator is the integral of the band in the absorbance spectrum, ρ_X is the density of absorbing molecules of a particular species in the mixture ($X = CH_4$ or C_2H_6), and L is the thickness of the ice layer.

On the other hand, A values can be obtained from the imaginary part of the refractive index, determined in the previous section, by means of the formula

$$A = \frac{4\pi}{\rho_X} \int_{band} v\, k(v)\, d(v). \qquad (2)$$

We have used densities of 0.45 g cm^{-3} for pure CH_4 at 18 and 30 K, and 0.41 or 0.54 g cm^{-3} for C_2H_6 ices at 18 and 30 K, respectively. For the (3:1), (1:1), and (1:3) mixtures we took 0.46, 0.50, and 0.50 g cm^{-3} at 18 K and 0.51, 0.55, and 0.58 g cm^{-3} at 30 K, respectively. All values were taken from
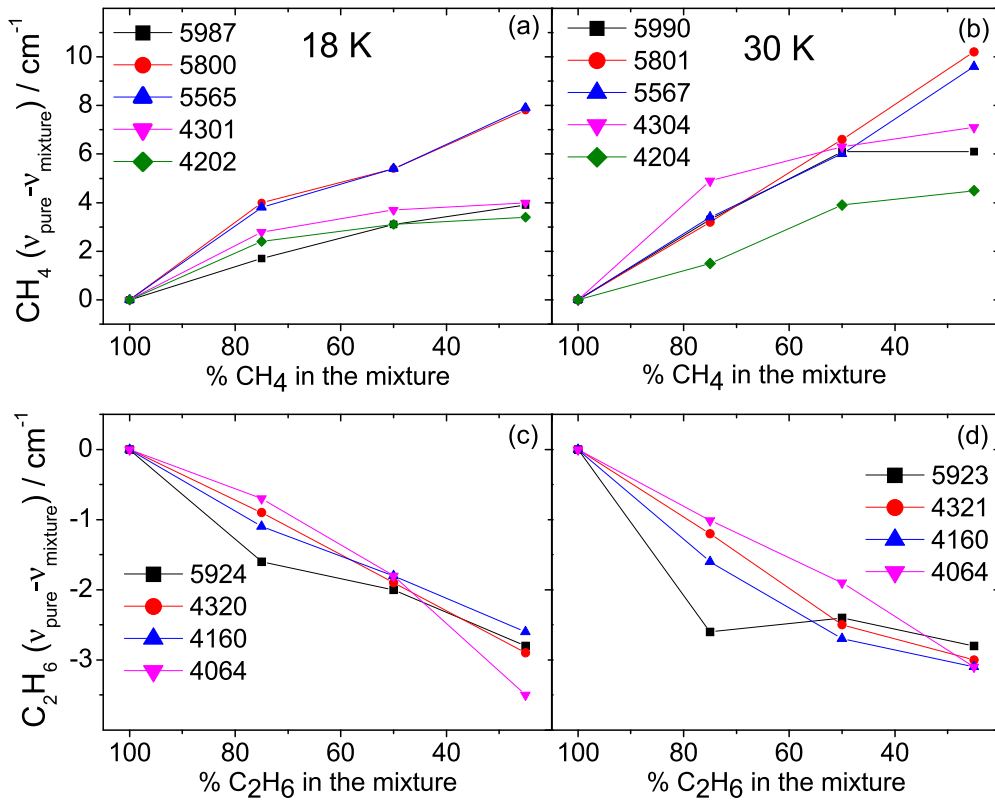
Figure 5. NIR methane (a, b) and ethane (c, d) band shifts ($\nu_{pure}-\nu_{mixture}$) in CH_4:C_2H_6 mixtures. A list with the peak positions for all bands and all mixtures is available. Data used to create this figure are available.

the measurements performed in this work. The numbers were converted to molecular densities by considering the fraction of each species in the mixture and their molecular weights (see Table 1, columns (2) and (5)). To determine the band strength of methane absorptions, the number of CH_4 molecules in the mixture was used (columns (3) and (6) in Table 1), and, in a similar way, for ethane absorptions we used the number of ethane molecules in the mixture (columns (4) and (7) in Table 1).

The band strengths obtained by applying Equation (1) are presented in Table 2 for methane and ethane bands, respectively. The values calculated using Equation (2), not listed here, differ from those in Table 2 by less than 15% for all cases at $T = 18$ K, except for the $1300\,cm^{-1}$, which deviates by $\sim$20%. At $T = 30$ K, these differences increase up to 25%. These variations can be expected since the magnitudes are evaluated using different procedures. However, the range of variation between A and A' is within our estimated experimental uncertainty, which we assess to be around 30%. This experimental error arises mainly in the integration process, where choices for baseline and band limits are particularly complicated in these mixtures where the bands of CH_4 and C_2H_6 appear very close and sometimes even overlap. Other sources of error lie in the determination of ice thickness, estimated to be less than 5%, and stoichiometry, well below 5%, thanks to the good reproducibility and stability provided by the mass flow controllers.

Figure 7(a) shows that the trend for methane band strengths for the NIR and MIR absorptions is to decrease with growing methane dilution in the mixture with respect to the values of the pure species. The average decay is below 30%, although in

particular the largest decay corresponds to the band at $4301\,cm^{-1}$, whose intensity drops by 65%. A similar tendency was found by Bossa et al. (2015) in CH_4:H_2O mixtures, where the CH_4 band strengths fall by 50% for water dilutions equivalent to the ethane dilutions in the present work. However, other previous investigations reveal contradictory results. The binary mixtures of methane with several volatiles (CO, CO_2, H_2O, N_2, O_2) studied by Hudgins et al. (1993), where methane is diluted by 20:1, show an increase in methane absorption intensity of the two main MIR bands. On the other hand, when methane is diluted in nitrogen in a (5:1) (N_2:CH_4) ratio, the intensity of its absorptions decays up to 90% (Gerakines et al. 2005; Richey & Gerakines 2012). All these studies make manifest that the different environments in various molecular ice mixtures modify the methane IR band intensities in dissimilar ways, probably related to the nature of the interactions between CH_4 and the other species. We have carried out theoretical simulations of the MIR spectra of CH_4:C_2H_6 mixtures that predict an intensity decline of the methane absorptions with increasing dilution in ethane, in agreement with the experiments. They will be discussed in Section 5.1.

For ethane, an intensity increase is observed for some of the IR absorption in the mixtures, and the opposite behavior for others. For example, the strong bands at 820 and $2880\,cm^{-1}$ become weaker upon methane dilution, while the one at $1369\,cm^{-1}$ strengthens. The number of vibrational modes of the ethane molecule is large, and the interactions among them in the molecular solid mixture should be quite complicated. Those interactions lead to the intensity modifications found in this study.
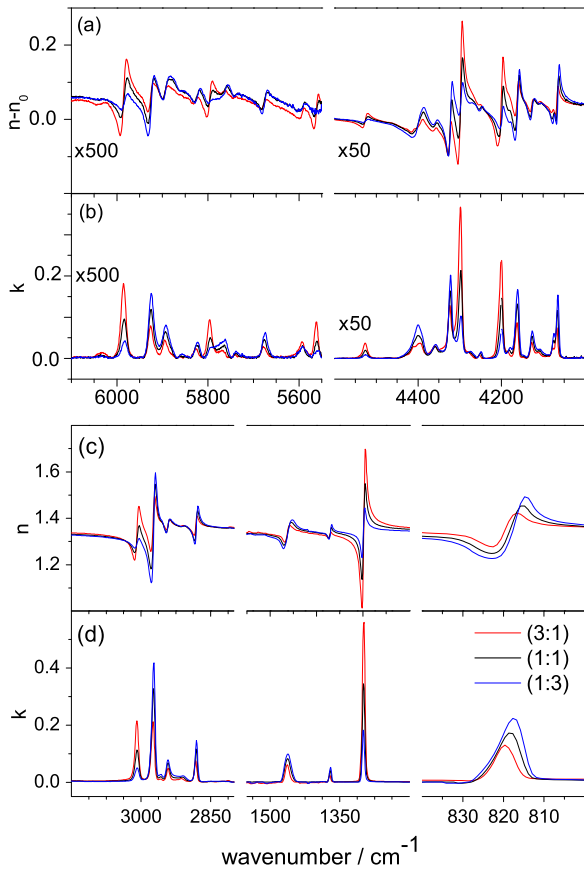
Figure 6. Optical constants of three mixtures of CH_4:C_2H_6 with proportions (3:1), (1:1), and (1.3) at 18 K. The numerical values of these optical constants and those at 30 K are available. Data used to create this figure are available.

Table 1
Molecular Densities of CH_4, C_2H_6, and CH_4:C_2H_6 Ices at 18 and 30 K

CH_4:C_2H_6	($\times 10^{22}$ molec cm^{-3})					
	18 K			30 K		
	ρ_{tot}	ρ_{CH_4}	$\rho_{C_2H_6}$	ρ_{tot}	ρ_{CH_4}	$\rho_{C_2H_6}$
(1:0)	1.69	1.69	0	1.69	1.69	0
(3:1)	1.42	1.07	0.36	1.57	1.18	0.39
(1:1)	1.31	0.66	0.66	1.44	0.72	0.72
(1:3)	1.14	0.29	0.86	1.32	0.33	0.99
(0:1)	0.82	0	0.82	1.08	0	1.08

There is an appreciable uncertainty in the experimental values, but it is of the same order for both species, and whereas for methane the intensities show a clear decaying pattern with increasing dilution for all bands, we do not observe a regular trend for ethane.

5. COMPARISON WITH PREVIOUS LITERATURE RESULTS

Several sets of optical constants in the MIR and NIR regions have been published over recent decades for methane ice (Roux et al. 1980; Pearl et al. 1991; Hudgins et al. 1993; Grundy et al. 2002; Bossa et al. 2015; Gerakines & Hudson 2015) and also for the band strengths of the main IR absorptions (d'Hendecourt & Allamandola 1986; Hudgins et al. 1993; Mulas et al. 1998; Brunetto et al. 2008; Bouilloud et al. 2015). Bouilloud et al. (2015) have made a compilation of these data. Comparison of the band strength values presented in their Table 6 with those in the third column of our Table 2 shows that the differences are between 7% and 20% (except for the strong ν_3 band at 3010 cm^{-1}, which is 40% weaker in some reports). The possible causes for these disagreements are commented on below.

All these previous investigations were carried out growing thin methane ice films (microns or thinner) by direct vapor deposition at lower temperature than that used in our experiments. Only in the work of Grundy et al. (2002) ices were generated by freezing the liquid phase in a cryogenic cell, obtaining ices several millimeters thick. Gerakines & Hudson

(2015) claim that their ices are the only amorphous methane samples, opposed to all previous literature results. To obtain that phase, they worked at 10 K and with a very low deposition rate (0.97 μm hr^{-1}). In this investigation we have grown the high-temperature, rather disordered crystalline phase I by deposition at 30 K and the crystalline phase II at 18 K. Figure 8 displays the imaginary part of the optical constants obtained in this work compared with some previous results. Even taking into account the various resolution values used in the different experiments, inspection of Figure 8 reveals the overall lower absorption strengths in our data than in former results. The most striking difference is found on the k index measured by Gerakines & Hudson (2015) for their amorphous ice, generated at very low temperature. It is well known that deposition temperature and growing rate influence the structure of the solid and therefore the intensity of the infrared absorptions. The disagreement found between our data and those of Gerakines & Hudson (2015) can be due to the fact that we have different methane ice phases.

There are other experimental details that need to be taken into account. It is now accepted that the deposition geometry determines the morphology of the sample (Dohnálek et al. 2003). Direct deposition leads to more compact deposits than background deposition, in which the molecules impinge the cold surface in all directions. In the present investigation the ice samples were grown by background deposition, and hence they may have a more porous structure than in the front-deposited samples used by other authors.

There is yet another issue that might cause an "overestimation" of the absorption coefficient in direct deposition experiments. In front deposition, if a multi-array doser is not used, the sample will not be built as a layer of homogeneous thickness, but it will present a conic form, thicker in the center than on the sides. Then, depending on the position where the He–Ne laser used to measure the thickness impinges on the sample, the thickness could be overestimated. Furthermore, if the capillary or the doser is not placed close enough to the cold surface, there could be a minor ice deposition on the back side of the substrate. If the interferometric technique of measuring the ice thickness is carried out in reflection configuration, this back-side deposit might not have been taken into account.

All these experimental reasons, plus possible intrinsic modifications of band strengths due to the presence of different phases and morphologies of the samples, could explain the discrepancies between the data in Figure 8.

The solid phases of ethane are also well characterized in the infrared. A recent work by Hudson et al. (2014) presents the MIR and NIR optical constants and band strengths of its three low-temperature phases, which agree well with previous literature

Table 2
Integrated Band Strength of the Main Absorption Features of CH_4 and C_2H_6 in the Pure Species and (CH_4:C_2H_6) Mixtures, at 18 and 30 K

CH_4					
Peak Position		A' (10^{-18} cm molec^{-1}) 18 K/30 K			
(cm^{-1})	(μm)	(1:0)	(3:1)	(1:1)	(1:3)
5987	1.670	0.036/0.024	0.035/0.025	0.033/0.028	0.033/0.32
5800	1.724	0.017/0.012	0.014/0.009	0.011/0.005	…
5565	1.797	0.011/0.007	0.009/0.007	0.009/0.009	−/0.006
4528	2.208	0.054/0.056	0.051/0.040	0.046/0.052	0.048/0.048
4301	2.325	0.560/0.492	0.335/0.184	0.292/0.240	0.257/0.119
4202	2.380	0.300/0.250	0.245/0.205	0.214/0.221	0.203/0.199
3010	3.322	9.402/10.227	8.610/6.799	6.767/5.834	6.140/5.467
1300	7.692	7.758/6.472	7.598/5.822	6.886/7.131	6.658/6.775
C_2H_6					
Peak Position		A' (10^{-18} cm molec^{-1}) 18 K/30 K			
(cm^{-1})	(μm)	(0:1)	(1:3)	(1:1)	(3:1)
5924	1.688	0.072/0.037	0.076/0.034	0.078/0.036	0.085/0.036
5673	1.763	0.013/0.012	0.012/0.013	0.01/0.014	0.011/0.014
5590	1.789	0.003/0.004	0.004/0.006	0.005/0.010	0.008/0.010
4400	2.273	0.283/0.256	0.298/0.242	0.235/0.236	0.244/0.209
4320	2.315	0.407/0.297	0.514/0.211	0.435/0.183	0.499/0.142
4160	2.404	0.218/0.118	0.233/0.185	0.199/0.183	0.226/0.172
4126	2.424	0.121/0.073	0.123/0.069	0.117/0.71	0.162/0.072
4064	2.461	0.167/0.166	0.167/0.169	0.164/0.176	0.191/0.150
2972	3.365	24.201/19.753	21.195/19.059	22.064/26.021	25.806/20.849
2880	3.472	2.778/1.959	4.251/3.871	4.657/4.953	5.585/4.262
2736	3.655	0.158/0.122	0.246/0.209	0.237/0.249	0.282/0.213
1461	6.845	3.918/3.772	3.924/3.686	3.673/4.501	4.328/3.541
1369	7.305	0.402/0.354	0.547/0.498	0.518/0.575	0.543/1.456
820	12.195	2.186/2.224	1.942/1.854	1.817/2.211	2.058/1.798

values. In our investigation only the amorphous phase was studied, grown by deposition at 18 K or 30 K. The imaginary k constant estimated in this work is compared with that of Hudson et al. (2014) in Figure 9. Our value for both the NIR and MIR is lower than theirs. For ethane ice we believe that porosity is taking an important role in deposition at low temperatures. We have measured a density of 0.41 and 0.54 g cm^{-3} for background-deposited ethane at 18 and 30 K, respectively, values clearly lower than that of crystalline ethane, 0.719 g cm^{-3}, as measured by Van Nes & Vos (1979). If we assumed a density of 0.719 g cm^{-3} for front-deposited amorphous ice at 20 K and of 0.41 g cm^{-3} for background-deposited ice (18 K), the band strengths obtained in the present work would transform to values that agreed within 5% with previous literature data.

5.1. Calculated MIR Spectra of Amorphous CH_4, C_2H_6, and (CH_4:C_2H_6) Ice Mixtures

With the methodology described in Section 2.2, we have calculated the spectra of the mixtures under study. The results are compared to the observed spectra in Figure 10. We can see that the degree of agreement is quite reasonable. The calculated spectra reproduce the main observed features, with slight deviations in relative intensities for absorptions in the whole MIR range, although the model tends to overestimate the intensities in the 1500–1300 cm^{-1} zone.

These theoretical models can also be used in an attempt to estimate spectroscopic effects in the mixtures, namely, intensity sharing or intensity transfer (Escribano et al. 2014 and

references therein). To that aim, we have built amorphous pure methane and pure ethane models in the same way as for the mixtures.

As is well known, molecular methane has two infrared active vibrations, ν_3 and ν_4, and two forbidden modes, ν_1 and ν_2 (although ν_2 can be seen in gas phase due to Coriolis interaction with ν_4). Our calculations for amorphous methane reproduce this scheme, with a slight activation of the forbidden modes due to the symmetry breaking arising from the amorphous arrangement of the molecules in the solid state (Hudson et al. 2015).

Table 3 lists the accumulated intensity per unit cell molecule, that is, the sum of the calculated intensities for a given mode divided by the number of carrier molecules of that mode within the unit cell. Thus, for the ν_3 mode of CH_4 the sum is carried out over all vibrations that display that character, divided by the number of methane molecules in the cell: 4, 3, or 2, for the pure species or mixtures with three or two methane molecules, respectively (columns (2)–(4) in the table). For this particular mode, there is a clear intensity drop along the series, in qualitative agreement with the observations collected in Table 2. However, no such tendency is predicted for ν_4, also in parallel with the experimental measurements.

For ethane, we list in Table 3 accumulated intensities for the five IR-active modes, ν_5, ν_6, ν_{10}, ν_{11}, and ν_{12}. Again, there is not a tendency in intensities for the series of mixtures, similarly to the experimental values.

Except for the ν_3 of methane and the ν_{10} of ethane, the intensity variations among the pure species and the mixtures do
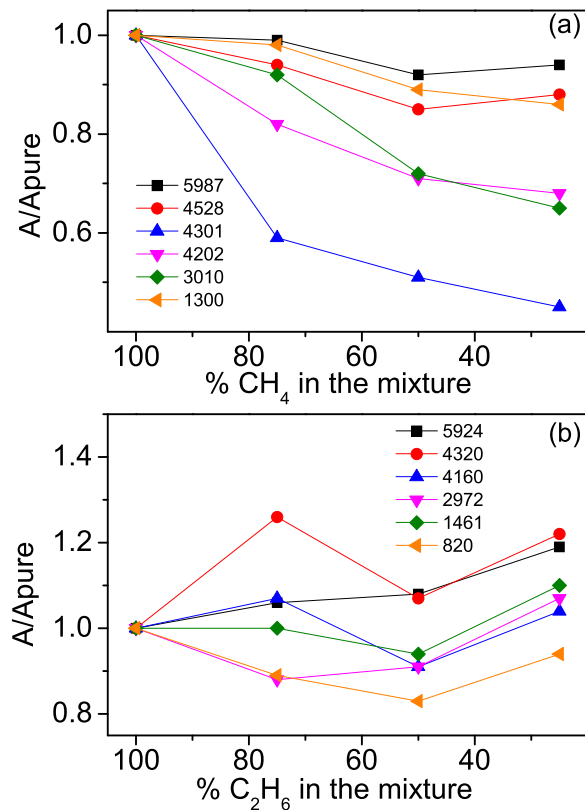
Figure 7. Relative variations of the integrated band strength of the main infrared absorptions of (a) CH$_4$ and (b) C$_2$H$_6$ in (CH$_4$:C$_2$H$_6$) mixtures at 18 K.

Figure 8. Imaginary part of the refractive index of CH$_4$ in some NIR (panels (a) and (b)) and MIR (panels (c) and (d)) spectral regions. Red trace in panel (a): Gerakines & Hudson (2015); panel (b): Grundy et al. (2002); panel (c): Gerakines & Hudson (2015); panel (d): Hudgins et al. (1993). Black trace in all panels: this work. The data behind this figure are available and also include the same data for ethane. Data used to create this figure are available.

not show a pattern that could be attributed to hypothetical interactions or coupling between modes. The most likely explanation points to distortions in the symmetry due to the environment within the amorphous solid. The intensity drop of the ν_3 of methane, on the other hand, seems to have a physical origin, which may indicate intensity transfer either to ν_1 of methane or to the strong ν_{10} of ethane, as could be deduced from the appearance of the spectra in Figures 4(a) and (b). A strong mode coupling, as predicted in polar environments (Escribano et al. 2014), is not observed in these samples, in which the most important intermolecular force is the dispersion force, very weak to induce strong activations. As a remark, we can say that the methodology employed seems to be suitable for the modeling of the IR features of this mixture.

6. SUMMARY AND ASTROPHYSICAL IMPLICATIONS

1. We have determined densities of pure methane and ethane ices and of three mixtures at 18 and 30 K. These magnitudes are essential to properly evaluate the band strengths of these species that are used to estimate their content in astrophysical media.
2. For amorphous ethane grown at 18 K or 30 K we have obtained a density of 0.41 and 0.54 g cm^{-3}, respectively, lower than a previous measurement of the density of the crystalline species, 0.719 g cm^{-3}. As far as we know, this is the first determination of the density of amorphous ethane ice. We found that when the appropriate density is used, the different porosity of the ices grown by diverse deposition techniques does not affect the intrinsic band strengths of the molecular absorptions.
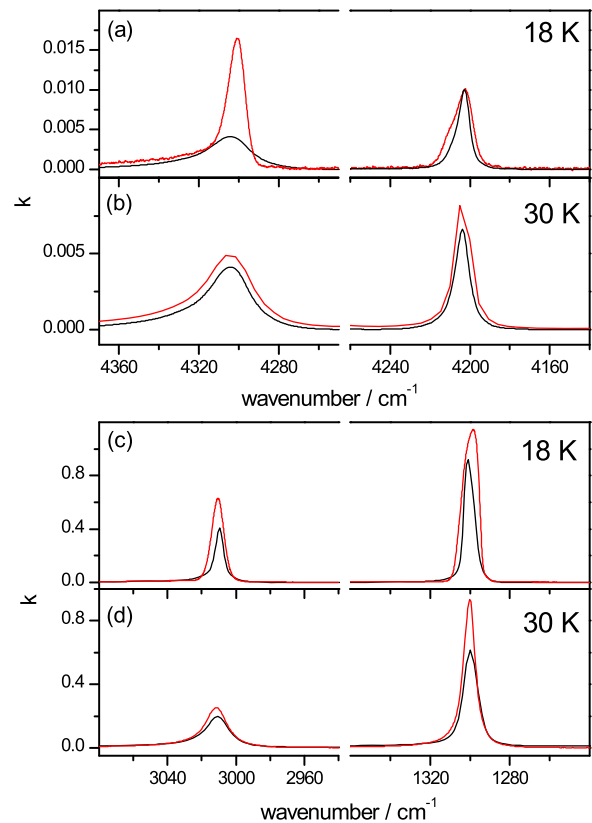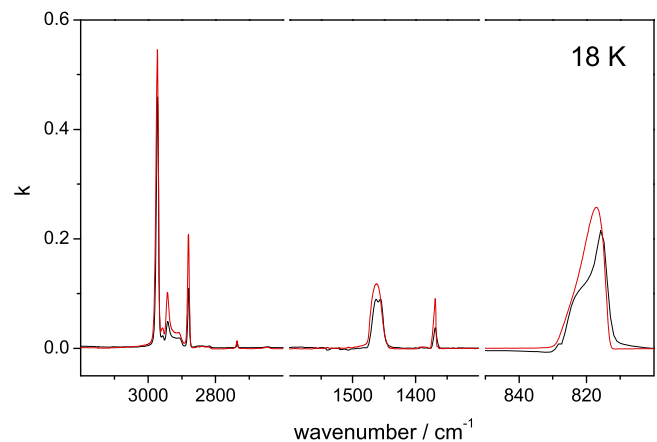

Figure 9. Imaginary part of the refractive index of C$_2$H$_6$ in some MIR spectral regions. Black trace: this work; red trace: data from Hudson et al. (2014).

3. We have estimated band strengths of the main NIR and MIR absorptions of methane and ethane. In general, intensity decay in methane modes was detected in the mixtures, whereas for ethane no clear tendency was observed. These values should be taken into account to quantify the amount of these species in TNOs' surfaces.
4. Optical constants of mixtures of methane and ethane at 30 and 18 K are given. They can be included in models to
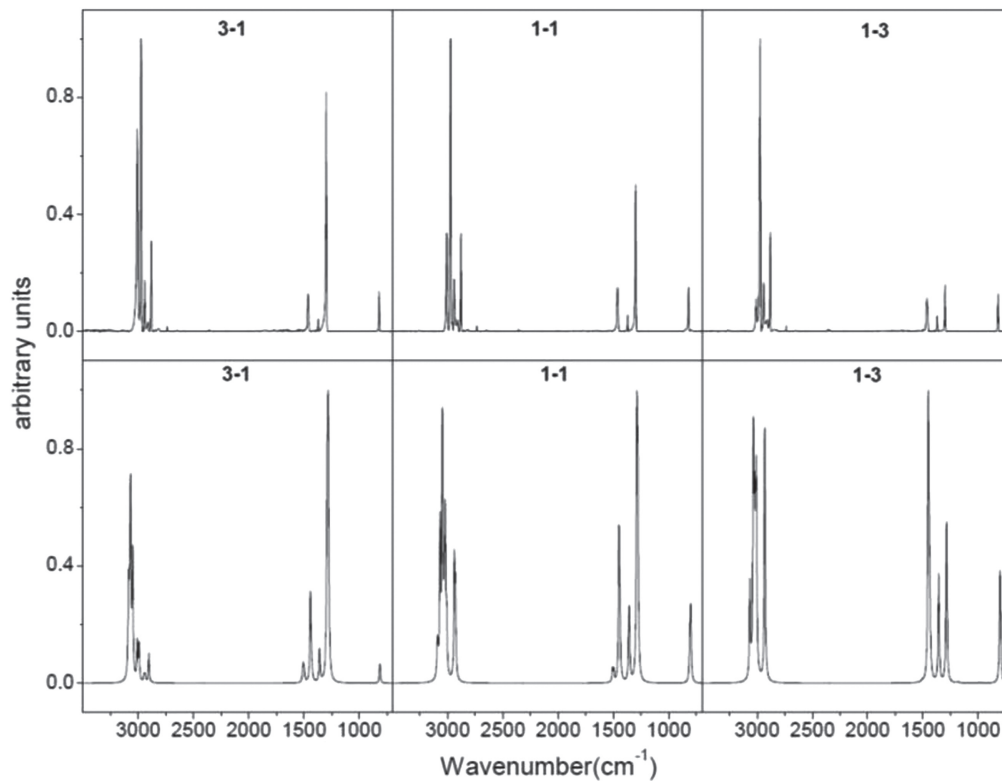
Figure 10. Experimental (top panel) and calculated (bottom panel) MIR spectra of the indicated CH_4:C_2H_6 mixtures. All the spectra are normalized to the most intense feature in order to compare both scales.

Table 3
Accumulated Intensity (km/mol) per Unit Cell Molecule for the Main MIR Methane Vibrations, for Pure CH_4 and CH_4:C_2H_6 and for Pure C_2H_6 and CH_4:C_2H_6 Mixtures

Pure CH_4 and CH_4:C_2H_6 Mixtures				
Vibrational Mode (Peak Position/cm^{-1})	(1:0)	(3:1)	(1:1)	(1:3)
ν_4 (1290)	137.47	83.94	96.46	60.65
ν_3 (3077)	121.52	78.18	60.40	34.44
Pure C_2H_6 and CH_4:C_2H_6 Mixtures				
Vibrational Mode (Peak Position/cm^{-1})	(0:1)	(1:3)	(1:1)	(3:1)
ν_{12} (809)	22.73	15.35	25.16	11.52
ν_6 (1365)	21.44	13.03	19.34	18.24
ν_{11} (1447)	61.98	46.98	44.31	61.56
ν_5 (2929)	27.24	16.13	41.85	29.99
ν_{10} (3026)	80.67	56.54	58.78	37.46

Note. Peak positions are referred to the pure species.

simulate TNOs' ice surfaces. With these values not only band shifts and band strengths are available, but also other spectral effects like macroscopic size and shape can be modeled. Furthermore, these results will allow the interpolation of the data to simulate mixtures of any methane/ethane ratios within the mixing intervals studied here.

5. We have proved that theoretical calculations at DFT level using solid-state software packages allow modeling the ice mixtures under study. These models reproduce satisfactorily the intensity decay observed in some mixtures.

6. We have measured band shifts of the main NIR methane and ethane features in the mixtures with respect to the corresponding values in the pure ices (see Figure 5 and supplementary material). These values can be used to trace the presence of these species in the surface of TNOs. For example, some observed features in the NIR spectra of Pluto match the strongest bands of pure ethane (2.27, 2.705, 2.457, 2.461 μm; 4405.3, 4158.0, 4070.0, 4063.4 cm^{-1}, respectively). On the other hand, a band at 2.317 μm (4315.9 cm^{-1}) in the spectrum of Pluto appears shifted with respect to a pure ethane measurement (2.315 μm; DeMeo et al. 2010). The ethane band at 2.315 μm moves to 2.313 μm (3 cm^{-1} shift) in the (3:1) mixture, farther away from the feature in Pluto's spectrum. Finally, a feature at 2.405 μm has been observed in some Pluto spectra (Nakamura et al. 2000; DeMeo et al. 2010), assigned mainly to CO, but which needs contribution from other species. The peak of pure ethane at 2.404 μm lies close by, but changes to 2.402 μm (4162.6 cm^{-1}) in a (3:1) mixture, in opposite direction to the observations. However, in the presence of different environments, the ethane band could be shifted in the right path.

7. The initial results of the *New Horizons* mission recently published by Stern et al. (2015) show a great variability on the characteristics of the surface of Pluto in color, morphology, or chemical composition. Pluto's surface has been known to contain N_2, CO, and CH_4. *New Horizons* reveals that this ice skin is masking the real water icy surface, and also the presence of old terrains with craters and ion-processed ices, in contrast with other younger surfaces with relatively high albedo, characteristic of nonprocessed ices. Colors reflecting this

variability could reveal tholins, or processed carbon-like chains. The results provided by this mission open the possibility of the occurrence of CH_4 segregation from nitrogen, as was previously suggested by Douté and collaborators (Douté et al. 1999).

The differences in ice composition among terrains should be related to atmosphere composition and evolution. LORRY and Alice data (Stern et al. 2015) of the atmospheric profile show N_2, CH_4, and also C_2H_x absorptions, the latter below 420 km. One of the most plausible explanations for the presence of C_2H_x in the atmosphere is that these molecules are formed by CH_4 processing in a methane-rich region on the surface. In order to obtain C_2H_x, methane ice should be segregated from the other volatiles, as otherwise the products of irradiation would bear nitrogen or oxygen in their composition. The formation of C_2H_x hydrocarbons from CH_4 irradiation is widely demonstrated in many experimental laboratories (de Vries et al. 1984; Kaiser & Roessler 1992; Strazzulla et al. 2002).

Some of these hydrocarbons, in particular C_2H_6 and C_2H_4, have also been detected from Earth observations made by Merlin (2015) with the ESO-VLT telescopes and the SINFONI instrument. All these evidences suggest that studies of mixtures of CH_4 and C_2H_x, as those provided in this article, may be helpful on the comprehension of chemical composition and evolution of Pluto's surface.

Additionally, information on these mixtures could be applied to other objects similar to Pluto. For example, Delsanti et al. (2010) studied the products of irradiation of CH_4 (and NH_3) in reference to the (90482) Orcus object. As they discussed in their article, there are many other TNOs of similar characteristics where processed CH_4 materials should be present. Similarly, Grundy et al. (2010) state that a patch of nonprocessed methane is compatible with the spectra of Triton, and Luna et al. (2012) proposed the different buoyancy between nitrogen and methane ices as the possible cause of this conclusion.

REFERENCES

Barucci, M. A., Cruikshank, D. P., Dotto, E., et al. 2005, A&A, 439, L1
Boogert, A. C. A., Schutte, W. A., Helmich, F. P., Tielens, A. G. G. M., & Wooden, D. H. 1997, A&A, 317, 929
Bossa, J.-B., Maté, B., Fransen, C., et al. 2015, ApJ, 814, 47
Boudin, N., Schutte, W., & Greenberg, M. 1998, A&A, 331, 749
Bouilloud, M., Fray, N., Benilan, Y., et al. 2015, MNRAS, 451, 2145
Brown, M. E., Barkume, K. M., Blake, G. A., et al. 2006, AJ, 133, 284
Brunetto, R., Caniglia, G., Baratta, G. A., & Palumbo, M. E. 2008, ApJ, 686, 1480
Clark, S. J., Segall, M. D., Pickard, C. J., et al. 2005, ZK, 220, 567
Clusius, K. 1929, ZPC, B3, 41
Cruikshank, D. P., Grundy, W. M., DeMeo, F. E., et al. 2015, Icar, 246, 82
Cruikshank, D. P., Pilcher, C. B., & Morrison, D. 1976, Sci, 194, 835
Dalle Ore, C. M., Barucci, M. A., Emery, J. P., et al. 2009, A&A, 501, 349
Dalton, J. B., Cruikshank, D. P., Stephan, K., et al. 2010, SSRv, 153, 113
Delsanti, A., Merlin, F., Guilbert-Lepoutre, A., et al. 2010, A&A, 520, A40
DeMeo, F. E., Dumas, C., de Bergh, C., et al. 2010, Icar, 208, 412
de Vries, A. E., Haring, R. A., Haring, A., Saris, F. W., & Pedrys, R. 1984, Natur, 311, 39
d'Hendecourt, L. B., & Allamandola, L. J. 1986, A&AS, 64, 453
Dohnálek, Z., Kimmel, G. A., Ayotte, P., Smith, R. S., & Kay, B. D. 2003, JChPh, 118, 364
Douté, S., Schmitt, B., Quirico, E., et al. 1999, Icar, 142, 421
Escribano, R., Timon, V., Gálvez, Ó, et al. 2014, PCCP, 16, 16694
Gálvez, O., Maté, B., Herrero, V. J., & Escribano, R. 2009, ApJ, 703, 2101
Gerakines, P. A., Bray, J. J., Davis, A., & Richey, C. R. 2005, ApJ, 620, 1140
Gerakines, P. A., & Hudson, R. L. 2015, ApJL, 805, L20
Grimme, S. 2006, JCoCh, 27, 1787
Grundy, W., Schmidt, B., & Quirico, E. 2002, Icar, 155, 486
Grundy, W. M., Young, L. A., Stansberry, J. A., et al. 2010, Icar, 205, 594
Hudgins, D. M., Sandford, S. A., Allamandola, L. J., & Tielens, A. G. 1993, ApJS, 86, 713
Hudson, R. L., Gerakines, P. A., & Loeffler, M. J. 2015, PCCP, 17, 12545
Hudson, R. L., Gerakines, P. A., & Moore, M. H. 2014, Icar, 243, 148
Kaiser, R. I., & Roessler, K. 1992, AnGeo, 10, 222
Licandro, J., Pinilla-Alonso, N., Pedani, M., et al. 2006, A&A, 445, L35
Luna, R., Satorre, M. Á, Domingo, M., Millán, C., & Santonja, C. 2012, Icar, 221, 186
Mastrapa, R. M., Bernstein, M. P., Sandford, S. A., et al. 2008, Icar, 197, 307
Merlin, F. 2015, A&A, 582, A39
Merlin, F., Barucci, M. A., de Bergh, C., et al. 2010, Icar, 210, 930
Mulas, G., Baratta, G. A., Palumbo, M. E., & Strazzulla, G. 1998, A&A, 333, 1025
Nakamura, R., Sumikawa, S., Ishiguro, M., et al. 2000, PASJ, 52, 551
Pearl, J., Ngoh, M., Ospina, M., & Khanna, R. 1991, JGR, 96, 17477
Perdew, J. P., Burke, K., & Ernzerhof, M. 1996, PhRvL, 77, 3865
Quirico, E., & Schmitt, B. 1997, Icar, 127, 354
Refson, K., Tulip, P. R., & Clark, S. J. 2006, PhRvB, 73, 155114
Richey, C. R., & Gerakines, P. A. 2012, ApJ, 759, 74
Roux, J. A., Wood, B. E., Smith, A. M., & Plyler, R. R. 1980, Infrared Optical Properties of Thin CO, NO, CH_4, HCl, N_2O, O_2, N_2, Ar, and Air Cryofilms (Arnold AFB, TN: Arnold Eng. Dev. Cent.)
Satorre, M. Á, Domingo, M., Millán, C., et al. 2008, P&SS, 56, 1748
Satorre, M. A., Leliwa-kopystynski, J., Santonja, C., & Luna, R. 2013, Icar, 225, 703
Schaller, E. L., & Brown, M. E. 2007, ApJL, 670, L49
Stern, S. A., Bagenal, F., Ennico, K., et al. 2015, Sci, 350, 1815
Strazzulla, G., Baratta, G. A., Domingo, M., & Satorre, M. A. 2002, NIMPB, 191, 714
Van Nes, G. J. H., & Vos, A. 1979, Acta Crys., B35, 2593
Wisnosky, M. G., Eggers, D. F., Fredrickson, L. R., & Decius, J. C. 1983, JChPh, 79, 3513
Zanchet, A., Rodriguez-Lazcano, Y., Galvez, O., et al. 2013, ApJ, 777, 26